Active flow control for external aerodynamics: from micro air vehicles to a full aircraft in stall

Journal of Physics: Conference Series **1522** (2020) 012017 doi:10.1088/1742-6596/1522/1/012017

Active flow control for external aerodynamics: from micro air vehicles to a full aircraft in stall

Oriol Lehmkuhl[1], Adrián Lozano-Durán[2], Ivette Rodriguez[3]

1 Dpt. of Computer Applications in Science and Engineering, Barcelona Supercomputing Center, Spain
2 Center for Turbulence Research, Stanford University, USA
3 Dpt. of Heat Engines, Universitat Politecnica de Catalunya, Spain

E-mail: oriol.lehmkuhl@bsc.es

Abstract. We investigate the aerodynamic performance of active flow control of airfoils and wings using synthetic jets with zero net-mass flow. The study is conducted via wall-resolved and wall-modeled large-eddy simulation using two independent CFD solvers: Alya, a finite-element-based solver; and charLES, a finite-volume-based solver. Our approach is first validated in a NACA4412, for which numerical and experimental results are already available in the literature. The performance of synthetic jets is evaluated for two flow configurations: a SD7003 airfoil at moderate Reynolds number with laminar separation bubble, which is representative of Micro Air Vehicles, and the high-lift configuration of the JAXA Standard Model at realistic Reynolds numbers for landing. In both cases, our predictions indicate that, at high angles of attack, the control successfully eliminates the laminar/turbulent recirculations located downstream the actuator, which increases the aerodynamic performance. Our efforts illustrate the technology-readiness of large-eddy simulation in the design of control strategies for real-world external aerodynamic applications.

1. Introduction

The overall performance of an aircraft wing is significantly affected by boundary-layer flow separation, specially at the high angles of attack (AoA) typically encountered during take-off and landing operations. In these situations, there is a loss of momentum across the boundary layer, which eventually leads to flow detachment. Thus, keeping the flow attached to the wing surface by supplementing additional momentum might improve the aerodynamic performance of the wing. In the quest for controlling or modifying the boundary layers over wings, different flow control strategies have been studied in the past years, namely, vortex generators, plasma actuators, synthetic jets, etc. (see the reviews in Refs. [1, 2, 3]). Here, we focus on the investigation of active flow control (AFC) of airfoils and wings for external aerodynamics via synthetic jets, which have been successful in reducing the fuel burnt during the operations of take-off and landing [4].

Significant advances have been achieved in the past years in the context of AFC in airfoils (see, for instance, [5, 6, 7, 8]), but whether such improvements are applicable to a full aircraft configuration remains an open question. A large body of studies have been conducted recently to explore the capabilities of AFC in high-lift devices. Shmilovich and Yadlin [9] studied different AFC strategies of a high-lift profile in the conditions of take-off and landing using the Reynolds-

Averaged Navier–Stokes equations (RANS). Bauer et al. [10] conducted experiments on a two element wing with unsteady AFC near the leading edge and showed that stall can be delayed. Lin et al. [11] addressed different strategies in the flap of a high-lift profile comprising steady suction and blowing, and periodic excitation of the boundary layer. Several of these AFC strategies are planned to be tested experimentally by NASA for increasing lift to drag ratios (L/D) in take-off configurations [12]. Recently, Andino et al. [13] tested fluidic actuators in a generic tail at low speeds and demonstrated that a modest increase of the momentum coefficient can result in important increments of the side force.

In the present work, we explore AFC of boundary layers in moderate-Reynolds-number airfoils and the wing of a full aircraft in high-lift configuration. The simulations are carried on using wall-resolved (WR) and wall-modeled (WM) large-eddy simulations (LES). The control approach adopted entails synthetic jets with zero net mass flux, in which the fluid necessary to alter the boundary layer is intermittently injected through an orifice driven by the motion of a diaphragm located on a sealed cavity below the surface [3]. Previous studies have shown that the periodic excitation introduced at the boundary layer by the jet has the potential to significantly change the lift and drag forces on airfoils and wings.

This paper is organized as follows. In §2, the modeling strategy is presented and validated with results in the literature for the NACA4412 at a chord-based Reynolds number of $Re_c = U_0 C/\nu = 10^6$ and $AoA = 5^o$ [14, 15]. Two different cases with AFC are proposed with increasing complexity. In §3, a SD7003 airfoil at $Re_c = 6\times10^4$ is studied with different actuations by means of wall-resolved LES. The objective is to understand the flow control of laminar separation bubbles, which is relevant for micro air vehicles and flaps of high-lift aircraft wings. In §4, the JAXA high-lift configuration Standard Model (JSM) is selected to investigate the performance of AFC on a full aircraft in stall conditions. A landing configuration with the high-lift devices (slat and flap) deployed in the absence of nacelle/pylon is considered at $Re_c = 1.93 \times 10^6$ and Mach number $M_\infty = 0.15$. Ten different actuations strategies are explored to assess the impact of the different control parameters. Finally, conclusions are offered in §5.

2. Mathematical modelling

We solve the spatially filtered Navier-Stokes equations,

$$\frac{\partial \overline{u}_i}{\partial x_i} = 0 \tag{1}$$

$$\frac{\partial \overline{u}_i}{\partial t} + \frac{\partial}{\partial x_j}(\overline{u}_j \overline{u}_i) = -\frac{\partial \overline{P}}{\partial x_i} + \frac{1}{Re}\nabla^2 \overline{u}_i - \frac{\partial \tau_{ij}}{\partial x_j}. \tag{2}$$

The variables are normalized using the reference length L and reference velocity U_0, which define the Reynolds number $Re = U_0 L/\nu$, where ν is the kinematic viscosity of the fluid. The filtered velocity is $\overline{u}_i$, $\overline{P} = \overline{p}/\rho$ is the modified pressure, and $\tau_{ij} = \overline{u_i u_j} - \overline{u}_i \overline{u}_j$ is the subgrid-scale stress (SGS) tensor. The SGS stresses tensor is modeled using an eddy viscosity approach with its deviatoric part parametrized as

$$\tau_{ij}^d = \tau_{ij} - \frac{\delta_{ij}}{3}\tau_{kk} = -2\nu_{\text{sgs}}\overline{S}_{ij} \tag{3}$$

where δ_{ij} is the Kronecker delta and

$$\overline{S}_{ij} = \frac{1}{2}\left(\frac{\partial \overline{u}_i}{\partial x_j} + \frac{\partial \overline{u}_j}{\partial x_i}\right) \tag{4}$$

is the strain-rate tensor. The formulation is closed by choosing a SGS viscosity, ν_{sgs}. In the present study ILSA [16] and Vreman [17] are used as SGS models.

The simulations are performed using two independent solvers. The first code, Alya [18], is a parallel multi-physics/multi-scale simulation code developed at the Barcelona Supercomputing Centre to run efficiently on high-performance computing environments. The convective term is discretized using a Galerkin finite element (FEM) scheme recently proposed [19], which conserves linear and angular momentum, and kinetic energy at the discrete level. Both second- and third-order spatial discretizations are used. Neither upwinding nor any equivalent momentum stabilization is employed. In order to use equal-order elements, numerical dissipation is introduced only for the pressure stabilization via a fractional step scheme [20], which is similar to those approaches used for pressure-velocity coupling in unstructured, collocated finite-volume codes [21]. The set of equations is integrated in time using a third-order Runge-Kutta explicit method combined with an eigenvalue-based time-step estimator [22]. This approach is significantly less dissipative than the traditional stabilized FEM approach [23].

A second set of simulations are conducted using the code charLES with a Voronoi mesh generator (Cascade Tech., Inc). The solver integrates the compressible LES equations using a second-order accurate finite volume formulation. The SGS model is the static-coefficient Vreman model. The numerical discretization relies on a flux formulation that is approximately entropy preserving in the inviscid limit, thereby limiting the amount of numerical dissipation added into the calculation. The time integration is performed with a third-order Runge-Kutta explicit method. The mesh generator is based on a Voronoi hexagonal close packed (HCP) point-seeding method which automatically builds high-quality meshes for arbitrarily complex geometries with minimal user input. First, the surface geometry of the aircraft is provided to describe the computational domain. Second, the the coarsest grid resolution is set to uniformly seeded HCP points.

To overcome the restrictive grid-resolution requirements to resolve the small-scale flow motions in the vicinity of the walls, we utilize a wall model. The no-slip boundary conditions at the walls are replaced instead by a wall-stress boundary condition. The wall-shear stress from the an algebraic equilibrium wall model is imposed as the wall boundary condition, and the wall is assumed to be isothermal. In the case of Alya, a finite element extension [24] of the wall law of Reichardt [25] is used:

$$u^+ = \frac{1}{\kappa}\ln\left(1+\kappa y^+\right) + 7.8\left(1 - \mathrm{e}^{-y^+/11} - \frac{y^+}{11}\mathrm{e}^{-0.33y^+}\right) \tag{5}$$

where $u_\tau = \tau_w^{1/2}$, $y^+ = yu_\tau/\nu$ and $u^+ = u/u_\tau$. For charLES, we use a simple algebraic wall model derived from the integration of the one-dimensional equilibrium stress model along the wall-normal direction,

$$u^+(y+) = \begin{cases} y^+ + a_1(y^+)^2 & \text{for } y^+ < 23, \\ \frac{1}{\kappa}\ln y^+ + B & \text{otherwise} \end{cases} \tag{6}$$

where $B = 5.2$ and a_1 is computed to ensure C^1 continuity. In charLES, the matching location for the wall model is the first off-wall grid cell of the LES mesh, and temporally filtered LES data are provided to the wall model as suggested by Yang et al. [26] to avoid the log-layer mismatch (LLM). Alya uses the exchange location suggested by Ref. [27]. The Navier–Stokes characteristic boundary condition for subsonic non-reflecting outflow is imposed at the outflow and top planes [28]. In all cases, we impose a uniform plug flow as the inflow boundary condition.

2.1. Wall modelling validation

Prior to the investigation of AFC strategies, we perform WMLES of a NACA4412 airfoil at $Re_c = U_0C/\nu = 10^6$ and $AoA = 5^o$ in order to validate the current modelling approach. The

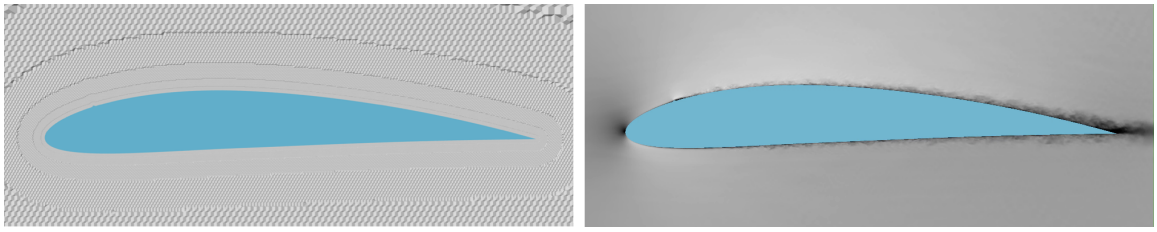

Figure 1. NACA4412 at $Re_c = 10^6$ and $AoA = 5^o$. Left: Voronoi grid. Right: instantaneous velocity magnitude. Results for charLES.

Reynolds number is defined in terms of the free-stream velocity U_0 and the airfoil chord C. This particular configuration has been recently studied by Vinuesa et al. [14] by means of wall-resolved LES using the spectral-element code Nek5000 and 2.28 billion grid points. Hence, the current case is a convenient testbed for LES under mild adverse pressure gradients (APG). We compare our results (the wall shear stress, boundary layer (BL) profiles, and pressure coefficient distribution) with Vinuesa et al. [14] and the experimental data available [15].

The simulations with Alya are carried out with a mesh of 6 million grid points, which is representative of WMLES [29]. The first off-wall grid point located at $y^+ \approx 30$, yielding roughly 10 elements within the BL region. Additionally, a bump of the size comparable to the BL thickness (δ) is placed at $x/C = 0.1$ to trigger the transition to turbulence similarly to previous experiments [15] and LES [14]. The ILSA SGS model [16] is used as eddy viscosity. For charLES, the mesh contains about 12 million degrees of freedom (DoF), and the SGS model selected is the Vreman model [17] with a constant coefficient equal to 0.1. A visualization of the Voronoi grid and the velocity magnitude for charLES is included in Figure 1.

The results for the wall-shear stress and the pressure coefficient are presented in Figure 2. No apparent differences are observed for the predictions obtained with WMLES compared to the experimental data [15]. Similar conclusions apply to the wall shear stress at the suction side. Although the results from WMLES do not show a fully turbulent BL until $x/C = 0.6$, the error relative to the wall resolved data is below 10% along the full chord. This outcome demonstrates the capabilities of WMLES in the presence of APG, even when equilibrium assumptions derived from mean zero-pressure-gradient boundary layers are invoked to model the near-wall region [30, 31].

The mean streamwise velocity profiles and the velocity fluctuations are assessed in Figure 3 at $x/C = 0.6, 0.7$ and 0.8. The results from Alya based, on an exchange location between WM and LES at the 3^{rd}-off grid node, shows a excellent agreement with the wall resolved data of Vinuesa et al. [14]. The results from charLES also show a good prediction of the mean velocity profile, although they exhibit a slight mismatch at the first grid points, which does not affect the prediction of the log layer further from the wall. Larger discrepancies are observed for the fluctuating velocities. The results from charLES are in fair agreement with the WRLES, but the results from Alya show a noticeable over prediction near the wall. These differences might be attributed to the coarser grid resolution used in the simulations with Alya (6M vs. 12 M DoF) [32]. Although they could also be due to the exchange location method utilized by Alya [27] in constant to the time filtering approach from charLES [26], or differences in the SGS model. A further assessment will be made in future works in order to clarify this issue.

3. Active flow control of airfoils with laminar separation bubbles

In this section, we focus on airfoils operating at moderate Reynolds numbers, which is of interest for the development of Micro Air Vehicles such as drones. To that end, we study the performance of different actuation mechanisms on the boundary layer of a SD7003 airfoil at

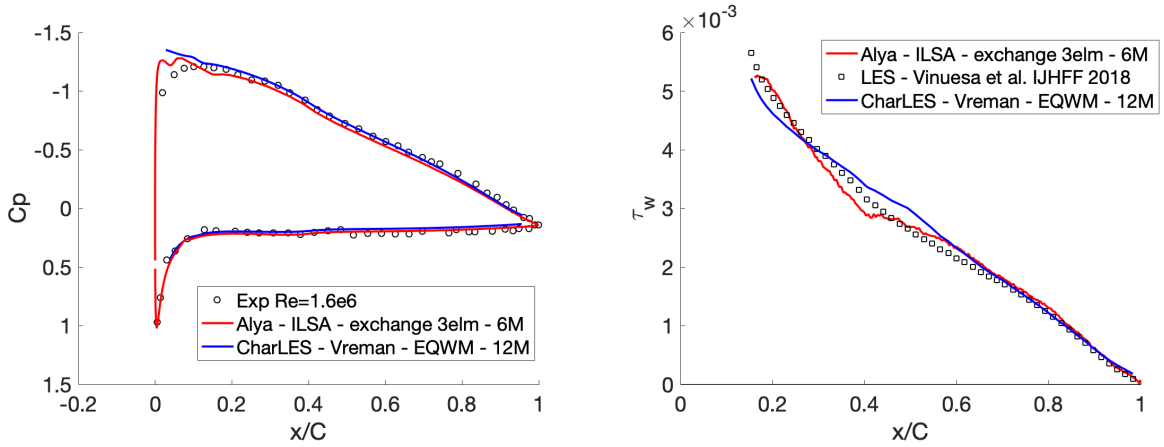

Figure 2. NACA4412 at $Re_c = 10^6$ and $AoA = 5^o$. left) Non-dimensional pressure at the airfoil surface, WMLES results vs. experimental data [15]. right) Wall shear stress at the suction side, WMLES results vs wall resolved results from Vinuesa et al. [14].

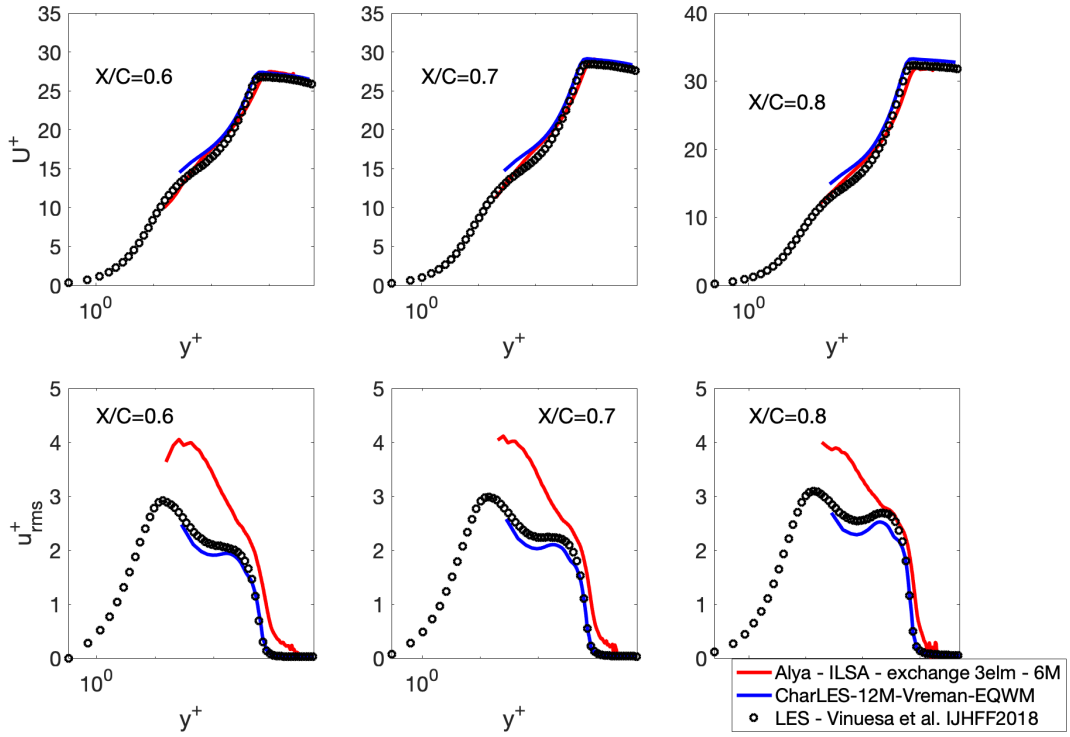

Figure 3. NACA4412 at $Re_c = 10^6$ and $AoA = 5^o$. top) Mean velocity profiles in wall units at position x/C = 0.6, 0.7 and 0.8, WMLES results vs wall resolved LES results from Vinuesa et al. [14]; bottom) RMS velocity profiles in wall units at position x/C = 0.6, 0.7 and 0.8, WMLES results vs wall resolved LES results from Vinuesa et al. [14]

$Re = U_0 C/\nu = 6 \times 10^4$. The Reynolds number is defined in terms of the free-stream velocity U_0 and the airfoil chord C. At the present moderate Re, the formation of a laminar separation bubble (LSB) may have a dominant effect on the flow field and thus, it is of prime importance to understand the role of the actuation on the reduction or suppression of the LSB along with the post-stall behavior. We consider three $AoAs$ equal to 4°, 11°, and 14°. The first AoA results in a large laminar separation bubble, the second is close to the maximum lift, while the last one corresponds with the flow in full stall.

For this part of the study we employ the solver Alya. Giving the moderate Reynolds number, the flow is simulated using wall-resolved LES. The dimensions of the computational domain are $15C \times 16C \times 0.2C$, with the leading edge of the airfoil placed at $(0, 0, 0)$. The boundary conditions at the inflow consist of a uniform velocity profile $(u, v, w) = (U_0 \cos(AoA),\, U_0 \sin(AoA), 0)$. For the outflow, we impose a pressure-based boundary condition. No-slip conditions on the airfoil surface are prescribed, and periodic boundary conditions are used in the spanwise direction. For the actuated cases, we impose the inlet velocity

$$(u, v, w)_{act} = A_p U_0 \sin(2\pi f t) \sin(2\pi\tau z)(\sin(AoA), \cos(AoA), 0). \tag{7}$$

Here, A_p is the maximum amplitude of the jet such that $U_{max} = A_p U_0$; f is the actuator frequency which defines $F^+ = f U_0 / x_{TE}$, with x_{TE} the distance from the actuator to the trailing edge; and τ is the spanwise period of the signal with $\tau = 0.5 L_z$. In the present simulations, a momentum coefficient $c_\mu = h(\rho U_{max}^2)/(C\rho U_0^2) = 3 \times 10^{-3}$ (with h the actuator width) and a non-dimensional frequency of $F^+ = 1$ are considered. The actuator outlet is located at $0.01C$. The computational meshes used for both the baseline and actuated cases are unstructured grids of about 30 million DoF. The meshes are obtained by extruding an unstructured two-dimensional mesh in $N_{elements}$ along the spanwise direction. The meshes are constructed to attain a wall-normal resolution of $\Delta y^+ \approx 1$ in the near wall region. The number of elements in the spanwise direction in all computations is 64.

With the aim of validating the current numerical set-up, the un-actuated case is compared with the available data in the literature obtained by Galbraith and Visbal [33] using implicit LES (ILES) with a computational grid of about 5.7 million grid points. A detailed comparison of the pressure coefficient and skin friction at $AoA = 4°$ and 11° is presented in Figure 4. In both cases, our results are in good agreement with Galbraith and Visbal [33], which provides confident in our current approach.

The lift and drag coefficients for both the actuated and baseline cases at $AoA = 4°, 11°$, and 14° are considered in Figure 5. Moreover, the instantaneous vortical structures represented by means of Q-isosurfaces for the baseline and the actuated cases are depicted in Figure 6. For an AoA lower than the point of maximum lift (i.e. $AoA = 11°$), the actuation successfully eliminates the laminar separation bubble and triggers the transition to turbulence right after the location of the actuator (see Figure 6). However, the new flow configuration offers no advantages from the airfoil efficiency point of view. Conversely, the airfoil efficiency increases considerably for the stall condition at $AoA = 14°$: the actuation increases the lift coefficient 19%, whereas the reduction in the drag forces is about 67%, thus increasing the airfoil efficiency by 98%. As can be seen from the Figure 6, in the baseline case for $AoA = 14°$, the flow massively separates from almost the leading edge of the airfoil and fails to reattach, producing a large recirculation bubble and momentum deficit in the suction side of the airfoil. As a consequence of the large detachment of the flow, the airfoil is stalled and its efficiency drops. When the actuator is activated, the jet transfers momentum to the flow and produces three-dimensional instabilities in the shear layer which trigger the transition to turbulence. The added momentum forces the shear layer to reattach to the airfoil surface for most of the airfoil chord. This results in a reduction in the separated zone of the airfoil and the increase in the airfoil efficiency.

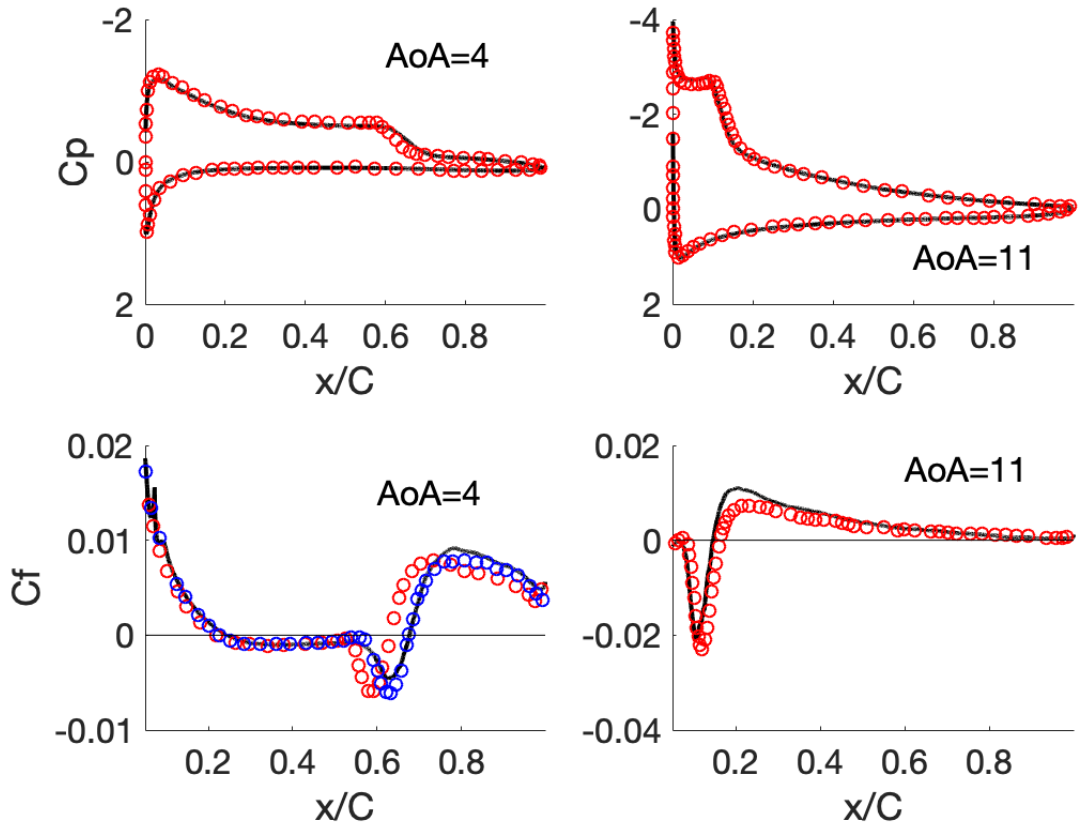

Figure 4. SD7003 at $Re_c = 6 \times 10^4$. Comparison with the literature. (solid line) present results. (blue circle) LES [34], (red circles) ILES [33]

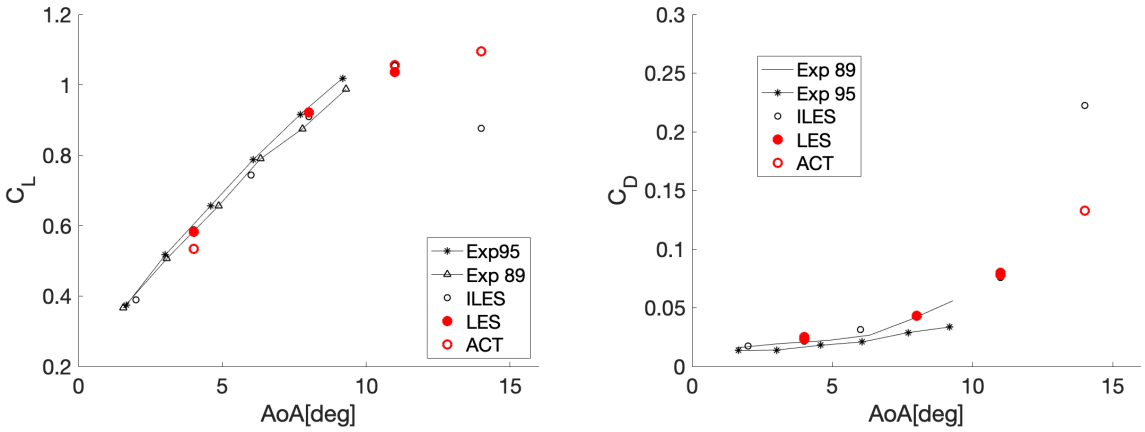

Figure 5. SD7003 at $Re_c = 6 \times 10^4$. Lift and drag coefficients for the controlled cases. Comparison with the baseline cases and with the literature.EXP95[35], EXP89[36], ILES[33].

4. Active flow control of a full aircraft in high-lift configuration at realistic Reynolds numbers

The JAXA Standard Model (JSM) in high-lift configuration, which was the experimentally studied at JAXA [37], is selected to investigate AFC strategies at realistic Reynolds numbers

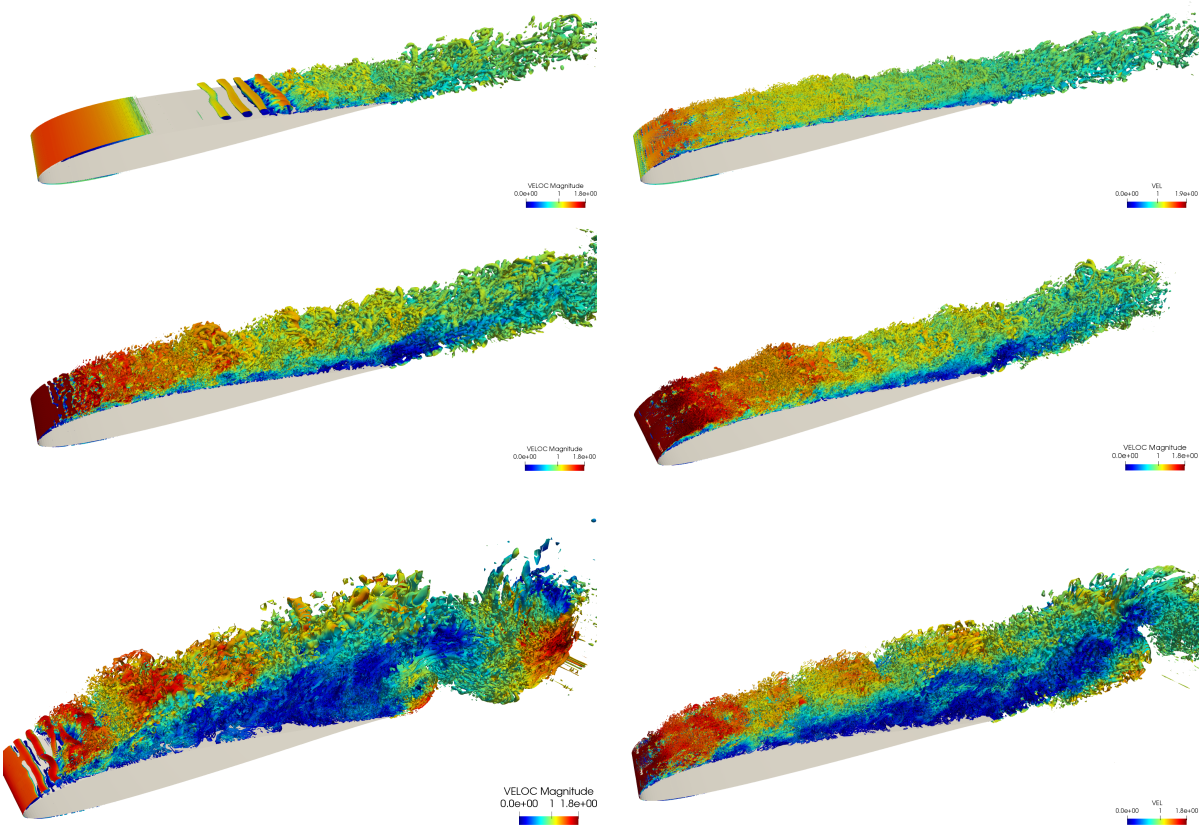

Figure 6. SD7003 at $Re_c = 6 \times 10^4$. Q iso-surfaces for the different configurations considered. Top left)$AoA = 4°$ baseline; top right) $AoA = 4°$ actuated; middle left) $AoA = 11°$ baseline; middle right) $AoA = 11°$ actuated; bottom left) $AoA = 14°$ baseline; and bottom right) $AoA = 14°$ actuated.

for a full aircraft. A landing configuration with the high-lift devices (slat and flap) deployed is considered at $Re_c = 1.93 \times 10^6$ and $M_\infty = 0.15$. The nacelle/pylon components are not included in the simulations. This geometry was the subject of study in the recent 3rd AIAA CFD High Lift Prediction Workshop [38], where various RANS-based methodologies were challenged to predict the onset of stall and maximum lift. The conclusions from the workshop pointed out the high sensitivity of the lift and drag results at high angle of attacks: RANS-based approaches exhibit multiple solutions given different initial conditions and they have difficulties to predict the lift coefficient at high AoA.

The study is mainly performed using Alya, and the most successful case is cross validated using charLES. The performance of WMLES in the JSM configuration has been previously assessed by Lehmkuhl et al. [39] at $AoAs$ pertaining to the linear-lift regime, maximum lift, and stall conditions (4, 10, 18.58, and 21.57 degrees). The results from the previous and the current validation exercise (Figure 7) reveal that the lift coefficient is in good agreement with the experimental results. The predicted drag is over estimated compared to the experimental measurements, although this may be due the geometric differences between the simulations and experimental set-up.

For the actuated cases, only the $AoA = 21.57°$ is considered in order to make the study computationally affordable. The meshes adopted are similar to those reported in Lehmkuhl et al. [39]. For Alya, the mesh consist of 180 millions of finite elements, and is composed of

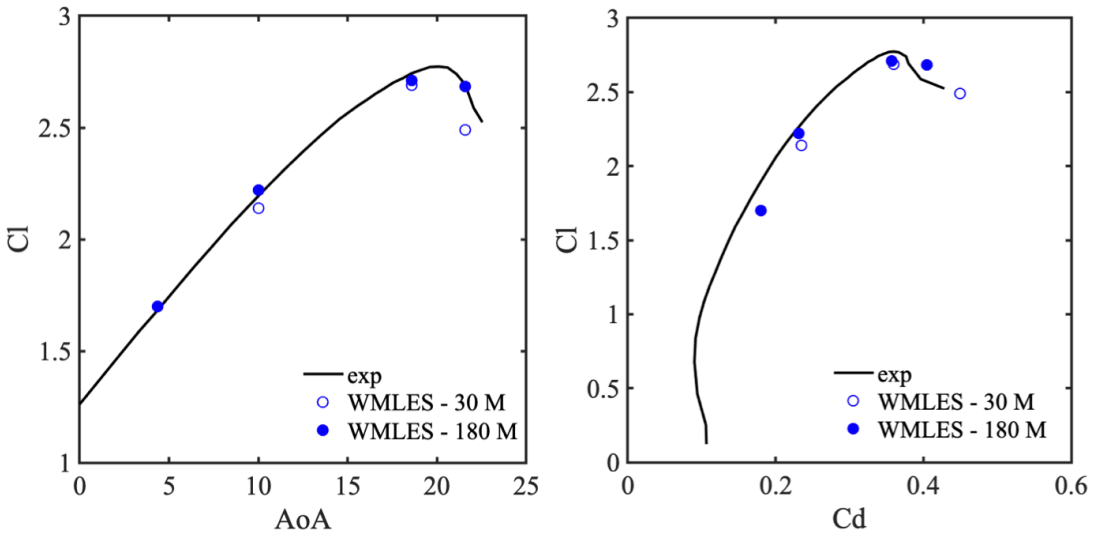

Figure 7. JSM high lift at $Re_c = 1.93 \times 10^6$. Averaged integral forces: WMLES vs experimental data[37, 40] (see Lehmkuhl et al. [39] for more details).

anisotropic wedge/prism layers near the wall and tetrahedra elsewhere. Additionally, dedicated mesh density zones are designed to provide a proper mesh resolution in the wakes of the slant, flap, and main wings. For charLES, the mesh is generated using a Voronoi grid with 60 millions control volumes and refinement close to the solid boundaries. The meshes are refined in the near-wall regions so that the number of grid cells across the local boundary layer thickness ranges from 5 to 10. The boundary conditions at the inflow consist of a uniform velocity profile $(u, v, w) = (U_0 \cos(AoA), 0, U_0 \sin(AoA))$. At outlet, a pressure-based boundary condition is imposed, while at the surface of the aircraft a wall stress boundary condition is imposed using the equilibrium model as described in §2. Homogeneous Neumann boundary conditions are used in the symmetry plane. The reader is referred to Lehmkuhl et al. [39] for more information about the current numerical set-up.

The actuation is imposed in the main wing and in the flaps as shown in the right panel of Figure 8x. The actuation is located at $x/C = 0.5$ for the main wing, and at $x/C = 0.1$ for the flap. Across the actuator area, we prescribe the jet velocity in x-, y- and z-direction as,

$$(u, v, w)_{act} = V_{max} \sin(2\pi f t) \cos(2\pi \tau_y y)(\cos\alpha, sin\alpha, 1)(\sin\Phi, \sin\Phi, \cos\Phi) \tag{8}$$

where f is the actuator frequency $F^+ = fC/U_0$, τ_y is the spanwise period of the signal (0 in 2D actuations and N_{jet}/L_y in 3D), V_{max} is obtained from $C_\mu = \frac{(\rho V_{max}^2) A_{act}}{(\rho V_0^2) A_{ref}}$, α is the angle with respect to the y-axis (see Figure 8 right) and Φ is the angle respect to the wing surface normal. The number of jets in the wing span(N_{jet}) is adjusted to have a $\tau_y = 0.1$. The main goal of the actuation is to control both the separation induced by the brackets connecting the slant and main wing, and the laminar separation bubbles in the flap region.

Ten actuation conditions are studied by varying the momentum coefficient, the actuation frequency, and the angle of actuator with respect to the normal direction to the surface. The complete test matrix is reported in Table 1. Three jet angles in the main wing are considered: normal (AFC1, AFC2, AFC3 and AFC4), tangential (AFC5, AFC6 and AFC7), and semi-tangential (AFC8, AFC9 and AFC10). The flap is always actuated with a jet in the normal direction to the surface. No actuation in the main wing is considered in AFC2 and AFC4. Following Shmilovich and Yadlin [9], the value of F^+ is set equal to 1.52. In AFC9, we select

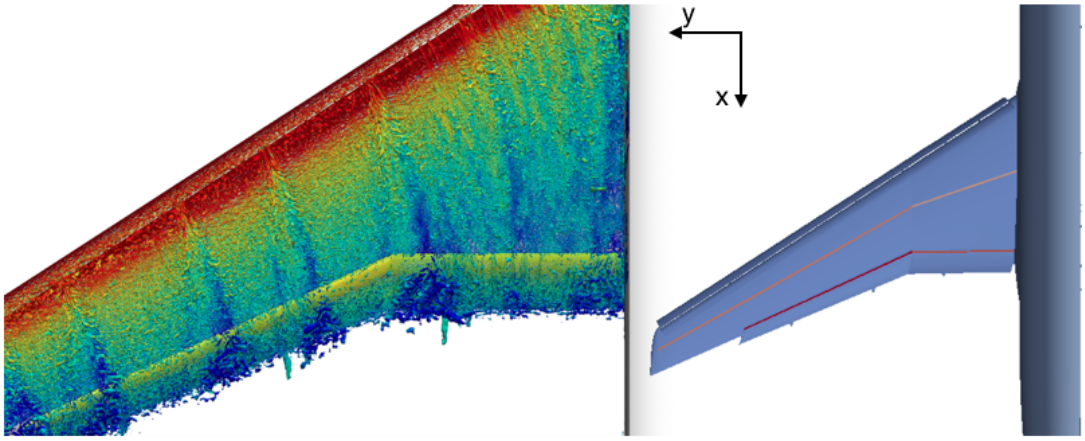

Figure 8. JSM high lift at $Re_c = 1.93 \times 10^6$ and $AoA = 21.57^o$. Left) Q iso-surfaces at the wing of JSM geometry colored by velocity magnitude (baseline case); right) x-y view: location of the synthetic jets (main at x/c = 0.5 and flap at x/c=0.1)

Table 1. JSM high-lift at $Re_c = 1.93 \times 10^6$ and $AoA = 21.57^o$. Considered AFC parameters.

		$\Phi[deg]$	C_μ	F^+	$3D/2D$
AFC1	main	0	0.015	1.52	3D
	flap	0	0.015	1.52	3D
AFC2	main	-	-	-	-
	flap	0	0.015	1.52	3D
AFC3	main	0	0.0075	1.52	3D
	flap	0	0.0015	1.52	3D
AFC4	main	-	-	-	-
	flap	0	0.0015	1.52	3D
AFC5	main	60	0.0075	1.52	2D
	flap	0	0.0015	1.52	3D
AFC6	main	60	0.015	1.52	2D
	flap	0	0.0015	1.52	3D
AFC7	main	60	0.0075	1.52	3D
	flap	0	0.0015	1.52	3D
AFC8	main	45	0.015	1.52	2D
	flap	0	0.0015	1.52	3D
AFC9	main	45	0.015	15.2	2D
	flap	0	0.0015	15.2	3D
AFC10	main	45	0.015/0.023	1.52	3D
	flap	0	0.0015	1.52	3D

$F^+ = 15.2$ to assess the effects of the frequency on the efficiency of the control. The impact of 2D actuation (constant C_μ) over the main wing is explored in cases AFC5, AFC6, AFC8 and AFC9. Finally a variable C_μ over the main wing to compensate for the change of spanwise area is assessed in AFC10.

The time-averaged aerodynamic forces are presented in Table 2. Since no experimental

results are available from the current control cases, we carried out an additional simulation of case AFC10 using charLES with a mesh of 60 millions control volumes. The predictions of C_L from Alya and charLES differ less than 1%, which cross validates the present approach using different numerical and modelling set-ups as described in section 2.1. Nonetheless, larger drag forces are predicted with charLES. This trend has been observed in the baseline configuration in previous simulations for the same JSM baseline flow configuration [39].

According to the results presented in Table 2, drag forces are reduced for all the proposed actuations at least by a 5%, while lift forces are improved only in AFC4, AFC5, AFC6, AFC8, AFC9 and AFC10. Even if the efficiency is improved by all the actuations considered, it is worth noting that, as a result of the periodic jets, the fluctuations in the drag and lift forces are considerably enhanced in all cases. This is accentuated for the case AFC9 ($F^+ = 15.2$), i.e., the periodic suction and blowing of the boundary layer produces a wave-like flow that alters the instantaneous values of the aerodynamic forces by more than one order of magnitude.

To understand the effect of the actuation on the main wing, we inspect the flow patterns in the presence and absence of actuation. Figure 9 shows the mean streamlines for the un-actuated base flow and for cases AFC3, AFC6, and AFC8. The visualizations suggest that the main losses in the lift forces are due to the formation of large separated zones. In the uncontrolled case, a large recirculation region occurs behind the flap, which lifts up the boundary layer in the rear end of the main wing right after the flow changes direction as induced by the flap deployment. For actuated cases with $\Phi = 0^\circ$ (AFC1 and AFC3), the turbulent boundary layer is vertically displaced, which decreases the lift coefficient. When the actuation in the main wing is suppressed, the variations in the lift is very small, and the jet located at the flap can barely act on the recirculation zone. The present results suggest that $\Phi = 0^o$ is not a viable option to improve the lift forces, and the most efficient actuations are in the tangential direction with angles between $\Phi = 45^o$ and $\Phi = 60^o$. For $\Phi = 45^\circ$, the jet is injected directly into the main boundary layer, enhancing mixing and preventing separation. The actuation strategies which approximates the best the ideal linear behavior of C_L are AFC8 and AFC10, with a slight improvement for case AFC10. In both cases, the large recirculation zone behind the flap is almost suppressed and the streamlines evolve parallel to each other behind the flap (see figure 9 bottom right and figure 10). Therefore, the actuator with spanwise-varying C_μ along the wing is effective in compensating for the geometrical changes in the wing.

5. Conclusions

Since the early days of aviation, many efforts have been devoted to the design of devices capable of providing the required lift, while reducing the associated drag of the device, such as slotted flaps or other high-lift mechanisms. Among the various approaches, active flow control via synthetic jets has emerged as a versatile technology for a broad range of applications at moderate and high Reynolds numbers. However, the use of CFD in the design of active flow control strategies for real-world applications has been hampered by the prohibitive computational cost associated with the computation of all the scales of the motions typically encountered in turbulent flows.

In the present work, we have investigated the impact of active flow control on the aerodynamic performance of actuated airfoils and wings. To make the problem tractable, the methodology employed has been wall-resolved and wall-modeled LES. Most of the simulations are carried out using the finite-element-based solver, Alya. To quantify the sensitivity of the results to the numerical discretization scheme, several cases have been simulated using a finite-volume-based solver, charLES.

Prior to the investigation of AFC with synthetic jets, we have validated the modelling capabilities of wall-modeled LES in a NACA4412 airfoil at $Re_c = 10^6$ and $AoA = 5^o$, for which high-fidelity CFD and experiments results are available in the literature. The simulation

Table 2. JSM high-lift at $Re_c = 1.93 \times 10^6$ and $AoA = 21.57^o$. AFC results.

		C_L	C_D	C_L/C_D	$C_{L_{rms}}$	$C_{D_{rms}}$
	Baseline	2.685	0.405	6.630	0.004	0.002
$\Phi = 0^o$	AFC1	2.574(−4.1%)	0.365(10.1%)	7.056(6.4%)	0.059	0.012
	AFC2	2.595(−3.4%)	0.359(11.4%)	7.226(9.0%)	0.046	0.011
	AFC3	2.668(−0.6%)	0.382(5.7%)	6.980(5.3%)	0.024	0.006
	AFC4	2.689(0.1%)	0.380(6.2%)	7.080(6.8%)	0.012	0.005
$\Phi = 60^o$	AFC5	2.695(0.4%)	0.380(6.2%)	7.096(7.0%)	0.051	0.023
	AFC6	2.719(1.3%)	0.385(4.9%)	7.072(6.7%)	0.063	0.029
	AFC7	2.685(0.0%)	0.380(6.2%)	7.075(6.7%)	0.015	0.005
$\Phi = 45^o$	AFC8	2.722(1.4%)	0.390(3.7%)	6.979(5.3%)	0.091	0.042
	AFC9	2.711(1.0%)	0.385(4.9%)	7.047(6.3%)	0.811	0.360
	AFC10	2.754(2.6%)	0.391(3.5%)	7.040(6.2%)	0.112	0.051
charLES	Baseline	2.640	0.460	-	-	-
	AFC10	2.740	0.480	-	-	-
Experiment[37]	Baseline	2.694	0.380	-	-	-

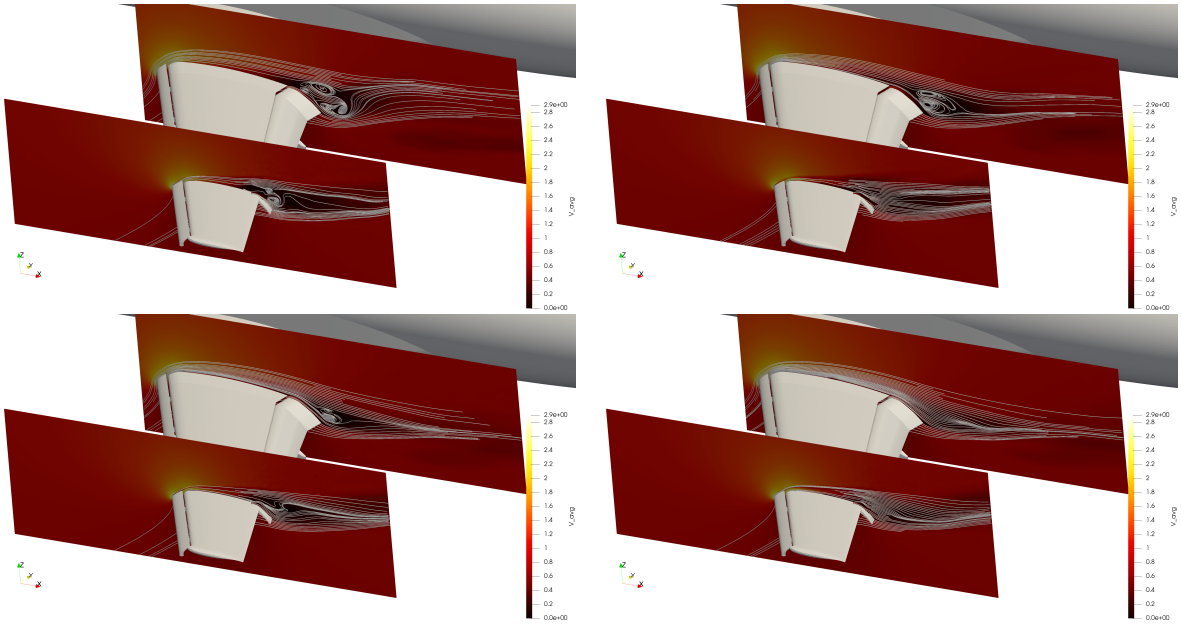

Figure 9. JSM high-lift at $Re_c = 1.93 \times 10^6$ and $AoA = 21.57^o$. 2D streamlines at different span-wise locations: baseline case vs different actuator jet angles. Top left) baseline; top right) AFC3($\Phi = 0^o$); bottom left) AFC6($\Phi = 60^o$); and bottom right) AFC8($\Phi = 45^o$).

are carried out using both solvers, Alya and charLES, with 6 millions DoF in the former and 12 million control volumes in the latter. Consistent with previous analysis, our results show that WMLES enables a faithful prediction of the most relevant figures of merit in external aerodynamics such as the pressure coefficient and skin friction, together with an accurate estimation of the mean velocity profile at multiple chord locations. The turbulence intensities are also correctly captured in the outer layer of the boundary layer, although they are overpredicted in the near-wall region with Alya. It was argued that several factors might be responsible for the overprediction of turbulence kinetic energy (grid resolution, wall-model matching location,

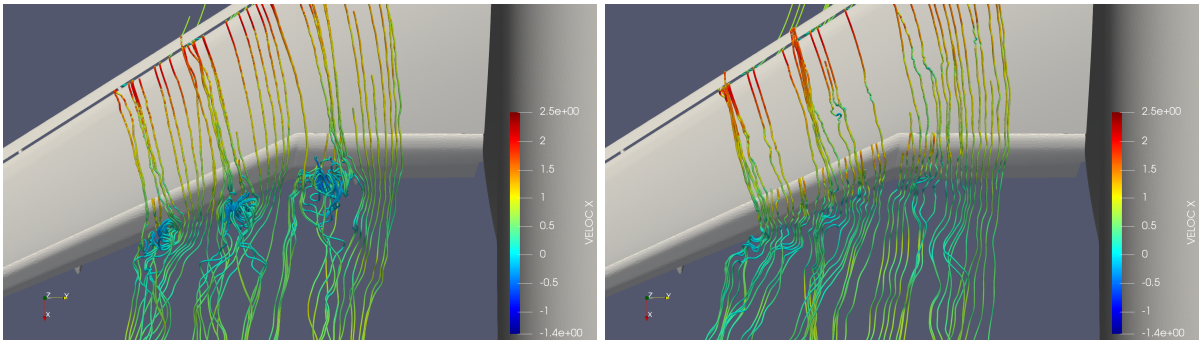

Figure 10. JSM high-lift at $Re_c = 1.93 \times 10^6$ and $AoA = 21.57^o$. Streamlines colored by non-dimensional streamwise velocity at the JSM high-lift wing: left) baseline configuration; right) AFC10.

SGS model,...), and future studies will be devoted to clarify this issue.

The effects of AFC in Micro Air Vehicles has been evaluated selecting as a representative case a SD7003 airfoil at $Re = U_0 C/\nu = 6 \times 10^4$. This flow configuration is characterized by a large separation bubble anchored at the leading edge of the airfoil, which is responsible for a degraded aerodynamic performance. The calculations are performed with Alya using wall-resolved LES with 30 million DoF. It is shown that actuating the airfoil in the vicinity to the leading edge at high AoA provides the necessary additional linear momentum to induce the breakdown of the laminar separation bubble. The new flow configuration is turbulent across the full chord of the airfoil, which improves considerably the aerodynamic performance. At lower $AoAs$, the synthetic jet is still able to suppress the laminar separation bubble, but with marginal improvements in terms of the aerodynamic performance.

The capabilities of AFC for a full aircraft in high-lift configuration at realistic Reynolds numbers is tackled by WMLES of the JAXA Common Research Model at $AoA = 21.57^o$ and $Re_c = 1.93 \times 10^6$. A systematic study of the effect of synthetic jets is addressed by performing a campaign of WMLESs varying the jet inclination angle relative to the solid boundary, the value of the momentum coefficient, actuating jet frequency, and the number of actuation lines (flaps or wing+flaps). The simulations are performed using Alya. The most successful case is also computed using charLES to provide cross-validation between different CFD solvers. Both Alya and charLES utilize the constant-coefficient Vreman SGS model and the algebraic equilibrium wall-model. The comprehensive matrix of cases provides rich information about the impact of the AFC on the flow. The most effective control in terms of aerodynamic performance (with 6.2% improvement) is achieved for jets with 45 degrees inclination angles, frequencies of $F^+ = 1.52$, and variable spanwise momentum coefficient along the wing. Interestingly, cases where the actuation is limited to the flaps reveal that the additional momentum injected into the boundary layer occurs too late downstream flow to efficiently remove the recirculation pattern.

The present analysis demonstrates the capabilities of LES to quantify the effects of active flow control for external aerodynamics. This ability to accurately predict turbulent flows without the necessity of empirical adjustments renders LES a promising methodology for arbitrary new geometries, as opposed to traditional Reynolds-Averaged Navier-Stokes (RANS) techniques which, require calibration according to the flow configuration.

Acknowledgment

This work is funded in part by the Coturb program of the European Research Council. O. L. acknowledges the financial support by the Ministerio de Economía y Competitividad, Secretaría de Estado de Investigación, Desarrollo e Innovación, Spain (ref. TRA2017-88508-R) and

the European Union's Horizon 2020 research and innovation programme (INFRAEDI-02-2018, EXCELLERAT- The European Centre Of Excellence For Engineering Applications H2020.). We also acknowledge Red Española de Supercomputación and Barcelona Supercomputing Center for awarding us access to the MareNostrum IV machine based in Barcelona, Spain (FI-2018-3-0021, FI-2018-2-0015, FI-2018-1-0022, FI-2017-3-0024). We acknowledge Prof. R. Vinuesa for the discussions and data analysis of the NACA4412. A.L.-D. acknowledges the support of NASA Transformative Aeronautics Concepts Program (Grant No. NNX15AU93A) and the Office of Naval Research (Grant No. N000141712310).We thank Prof. Philipp Schlatter for reading the manuscript and for his valuable suggestions.

References

[1] T. C. Corke, C. L. Enloe, and S. P. Wilkinson. Dielectric barrier discharge plasma actuators for flow control. *Ann. Rev. Fluid Mech.*, 42:505–529, 2010.
[2] L. N. Cattafesta and M. Sheplak. Actuators for active flow control. *Ann. Rev. Fluid Mech*, 43(1):247–272, 2011.
[3] A. Glezer. Some aspects of aerodynamic flow control using synthetic-jet actuation. *Phil. T. Roy. Soc. A*, 369:1476–1494, 2011.
[4] P. M. Hartwich, A. Shmilovich, D. S. Lacy, E. D. Dickey, A. J. Scalafani, P. Sundaram, and Y. Yadlin. Refined AFC-enabled high-lift system integration study. Technical Report NASA/CR-2016-219170, 2016.
[5] D. C. Mccormick. Boundary layer separation control with directed synthetic jets. In *38th AIAA Aerospace Sciences Meeting & Exhibit*, number 2000-0519, 2000.
[6] M. Amitay and A. Glezer. Role of actuation frequency in controlled flow reattachment over a stalled airfoil. *AIAA J.*, 40:209–216, 2002.
[7] J. L. Gilarranz, L. W. Traub, and O. K. Rediniotis. A new class of synthetic jet actuators–Part I: Design, fabrication and bench top characterization. *J. Fluids Eng.*, 127:367–376, 2005.
[8] D. You and P. Moin. Active control of flow separation over an airfoil using synthetic jets. *J. Fluids Struct.*, 24:1349–1357, 2008.
[9] A. Shmilovich and Y. Yadlin. Active flow control for practical high-lift systems. *J. Aircraft*, 46:1354–1364, 2009.
[10] M. Bauer, J. Lohse, F. Haucke, and W. Nitsche. High-lift performance investigation of a two-element configuration with a two-stage actuator system. *AIAA J.*, 52:1307–1313, 2014.
[11] J. C. Lin, L. G. Pack Melton, S. Viken, M. Y. Andino, M. Koklu, J. Hannon, and V. N. Vatsa. High Lift Common Research Model for Wind Tunnel Testing: An Active Flow Control Perspective. In *55th AIAA Aerospace Sciences Meeting*, number 2017-0319, 2017.
[12] J. C. Lin, L. G. Pack Melton, J. Hannon, M. Y. Andino, M. Koklu, K. Paschal, and V. N. Vatsa. Wind tunnel testing of active flow control on the high-lift common research model. In *AIAA Aviation 2019 Forum*, number 2019-3723, 2019.
[13] M. Y. Andino, J. C. Lin, S. Roman, E. C. Graff, M. Gharib, E. A. Whalen, and I. J. Wygnanski. Active flow control on vertical tail models. *AIAA J.*, 57:3322–3338, 2019.
[14] R. Vinuesa, P.S. Negi, M. Atzori, A. Hanifi, D.S. Henningson, and P. Schlatter. Turbulent boundary layers around wing sections up to $Re_c = 1000000$. *Int. J. Heat Fluid Flow*, 72:86–99, 2018.
[15] R. C. Hastings and B. R. Williams. Studies of the flow field near a NACA 4412 aerofoil at nearly maximum lift. *Aeronaut. J.*, 91(901):29–44, 1987.
[16] O. Lehmkuhl, U. Piomelli, and G. Houzeaux. On the extension of the integral length-scale approximation model to complex geometries. *Int. J. Heat Fluid Flow*, 78:108422, 2019.
[17] A. W. Vreman. An eddy-viscosity subgrid-scale model for turbulent shear flow: Algebraic theory and applications. *Phys. Fluids*, 16:3670–3681, 2004.
[18] A. M. Vazquez, G. Houzeaux, S. Koric, A. Artigues, J. Aguado-Sierra, R. Aris, D. Mira, H. Calmet, F. Cucchietti, H. Owen, E. Casoni, A. Taha, E. D. Burness, J. M. Cela, and M. Valero. Alya: Multiphysics engineering simulation towards exascale. *J. Comput. Sci.*, 14:15–27, 2016.
[19] S. Charnyi, T. Heister, M. A. Olshanskii, and L. G. Rebholz. On conservation laws of Navier-Stokes Galerkin discretizations . *J. Comput. Phys.*, 337:289 – 308, 2017.
[20] R. Codina. Pressure stability in fractional step finite element methods for incompressible flows. *J. Comput. Phys.*, 170:112–140, 2001.
[21] L. Jofre, O. Lehmkuhl, J. Ventosa, F.X. Trias, and A. Oliva. Conservation properties of unstructured finite-volume mesh schemes for the Navier-Stokes equations. *Numer. Heat Tr. B–Fund.*, 65:53–79, 2014.

[22] F. X. Trias and O. Lehmkuhl. A self-adaptive strategy for the time integration of Navier-Stokes equations. *Numer. Heat Tr. B–Fund.*, 60:116–134, 2011.
[23] O. Lehmkuhl, G. Houzeaux, H. Owen, G. Chrysokentis, and I. Rodriguez. A low-dissipation finite element scheme for scale resolving simulations of turbulent flows. *J. Comput. Phys.*, 390:51 – 65, 2019.
[24] H. Owen, G. Chrysokentis, M. Avila, D. Mira, G. Houzeaux, R. Borrell, J. C. Cajas, and O. Lehmkuhl. Wall-modeled large-eddy simulation in a finite element framework. *Int. J. Num. Meth. Fluids*, 2019.
[25] H. Reichardt. Vollständige darstellung der turbulenten geschwindigkeits- verteilung in glatten leitungen. *ZAMM-Z. Angew. Math. Me.*, 31:208–219, 1951.
[26] X. I. A. Yang, G. I. Park, and P. Moin. Log-layer mismatch and modeling of the fluctuating wall stress in wall-modeled large-eddy simulations. *Phys. Rev. Fluids*, 2:104601, 2017.
[27] S. Kawai and J. Larsson. Wall-modeling in large eddy simulation: Length scales, grid resolution, and accuracy. *Phys. Fluids*, 24(015105), 2012.
[28] T. J. Poinsot and S. K. Lele. Boundary conditions for direct simulations of compressible viscous flows. *J. Comput. Phys.*, 101:104 – 129, 1992.
[29] A. Lozano-Durán and H. J. Bae. Error scaling of large-eddy simulation in the outer region of wall-bounded turbulence. *J. Comput. Phys.*, 392:532–555, 2019.
[30] J. Larsson, S. Kawai, J. Bodart, and I. Bermejo-Moreno. Large eddy simulation with modelled wall stress: recent progress and future directions. *Mech. Eng. Rev.*, 3, 2016.
[31] S. T. Bose and G. I. Park. Wall-modeled large-eddy simulation for complex turbulent flows. *Annu. Rev. Fluid Mech.*, 50:535–561, 2018.
[32] H. J. Bae, A. Lozano-Durán, S. T. Bose, and P. Moin. Turbulence intensities in large-eddy simulation of wall-bounded flows. *Phys. Rev. Fluids*, 3:014610, 2018.
[33] M. Galbraith and M. Visbal. Implicit large eddy simulation of low Reynolds number flow past the SD7003 airfoil. In *46th AIAA Aerospace Sciences Meeting and Exhibit*, number 2008-225, 2008.
[34] S. Schmidt and M. Breuer. Hybrid LES-URANS methodology for the prediction of non-equilibrium wall-bounded internal and external flows. *Comput. Fluids*, 96:226–252, 2014.
[35] M. S. Selig, J. J. Guglielmo, A. P. Broeren, and P. Giguere. Summary of low-speed airfoil data. Technical report, University of Illinois, 1995.
[36] M. S. Selig, J. F. Donovan, and D. B. Fraser. Airfoils at low speeds. Technical report, University of Illinois, 1989.
[37] Y. Yokokawa, M. Murayama, M. Kanazaki, K. Murota, T. Ito, and K. Yamamoto. Investigation and improvement of high-lift aerodynamic performances in low speed wind tunnel testing. *AIAA Pap.*, (2008-350), 2008.
[38] C. L. Rumsey, J. P. Slotnick, and A. J. Sclafani. Overview and summary of the Third AIAA High Lift Prediction Workshop. *AIAA Pap.*, (2018-1258. Also, https://hiliftpw.larc.nasa.gov/), 2018.
[39] O. Lehmkuhl, G. Park, S.T. Bose, and P. Moin. Large-eddy simulation of practical aeronautical flows at stall conditions. In *Center Turb. Res.–Proc. Summer Prog.*, pages 87–96, 2018.
[40] Y. Yokokawa, M. Murayama, H. Uchida, K. Tanaka, T. Ito, and K. Yamamoto. Aerodynamic influence of a half-span model installation for high-lift configuration experiment. *AIAA Pap.*, (2010-684), 2010.